

Enhancing the relative capture width of submerged point absorbing wave energy converters

Boyin Ding¹, Nataliia Sergiienko², Fantai Meng³, Benjamin Cazzolato, Peter Hardy, and Maziar Arjomandi

*Ocean Wave Energy Research Group, School of Mechanical Engineering, the University of Adelaide
South Australia, Australia, 5005*

¹boyin.ding@adelaide.edu.au

²nataliia.sergiienko@adelaide.edu.au

³fantai.meng@adelaide.edu.au

Abstract— Point absorbing wave energy converters account for 53% of the existing wave energy converter prototype designs. Generally, point absorbers are designed to operate on or just below the water surface, extracting wave power from the heaving motion. In recent years, an increasing amount of attention has been given to fully submerged point absorbers that demonstrate better survivability under storm conditions and capability of extracting wave power from motion in multiple degrees of freedom. This paper investigates three submerged point absorber designs operating in three degrees of freedom: a generic axisymmetric spherical buoy with a single tether power-take-off; and two modified types, one employing an asymmetric mass distribution buoy and the other employing a three tether power-take-off arrangement. Simulations in the frequency domain were used to study the behaviour of the three point absorber designs from the perspectives of dynamic response, power absorption principles and capabilities, and power-take-off requirements. Compared to the generic single tether spherical buoy design, both modified submerged point absorber designs demonstrate considerable improvements in their performance indices (e.g. the relative capture width and the power to PTO force ratio), while exhibit additional challenges in their implementations.

Keywords— Point absorber, submerged wave energy converter, multiple degrees of freedom oscillation, optimal power-take-off

I. INTRODUCTION

Ocean wave energy has been under the public spotlight over the past few decades for its high energy density, predictability, and consistency. It has shown a great potential to address the increasing global energy demand, with recent estimates suggesting a global wave energy capacity exceeding 2TW [1]. However, wave energy converter (WEC) technologies that extract energy from ocean waves are still in their pre-commercial phase and exhibit great diversity in design, leading to more than one thousand different WEC prototypes in various stage of development [2].

Oscillating point absorbing wave energy converters (PAs), a popular type of WEC designs defined by having geometry smaller than a wavelength, account for 53% of the existing WEC prototypes [3]. PAs are usually designed as axisymmetric buoys which are insensitive to wave direction change [1]. They typically operate offshore in deep water waves with higher energy content than shallow water waves [4]. Budal and Falnes [5], and Evans [6] found that given unconstrained motion, the

maximum capture width of the oscillating body does not depend on its size, shape or submergence depth, but is only governed by the mode of motion. An axisymmetric body needs to oscillate in at least two modes, one radiating symmetric waves such as heave and the other radiating antisymmetric waves such as surge, to absorb the maximum available power from waves [7], [8].

Sergiienko et al. [9] compared the power absorption capability of floating and fully submerged PAs under physical motion constraints [9]. Results showed that in comparison with floating PAs, fully submerged PAs generally absorb less power from the heaving mode, but absorb similar amount of power from the combined heaving and surging modes. Furthermore, fully submerged PAs experience less wave excitation force and therefore exhibit higher durability and survivability than floating counterparts. Therefore, a submerged PA operating in multiple degrees of freedom has a potential to resolve the trade-off between power absorption capability and survivability in WEC design.

Buoys are typically submerged in water by a single tether anchored to the seabed (bottom-reference [10]) with a power-take-off (PTO) machinery installed along the tether that converts mechanical power due to buoy oscillation into electricity, as illustrated in Fig. 1(a). Anchored by a tether and excited by a plane wave, the buoy is able to move in three degrees of freedom (3DoF), namely heave, surge and pitch [11]. However, the majority of the wave power is absorbed from the buoy's heave motion arising from the kinematic constraint of the single tether PTO arrangement, where PTO is aligned with the heave motion predominantly. The authors of this paper have previously investigated two submerged PA design variants that are capable of extracting wave energy from the buoy's 3DoF oscillations. The first prototype employs a buoy with asymmetric mass distribution as shown in Fig. 1(b), with the

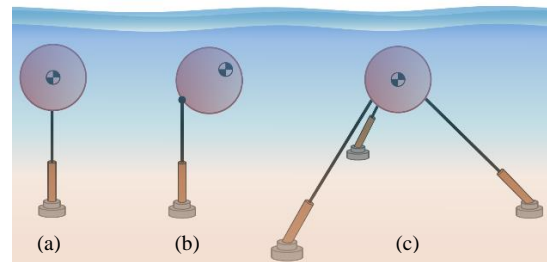


Fig. 1 Tether anchored (bottom fixed) submerged point absorber variants

goal of enhancing dynamic coupling between the buoy's oscillating modes and consequently absorbing power from surge by exploiting the surge-pitch and pitch-heave couplings [12]. The second prototype applies a three-tether PTO arrangement in tripod formation as shown in Fig. 1(c), originally proposed by Srokosz in 1979 [13]. The three-tether PTO can enhance kinematic coupling between the buoy's oscillating modes and the PTO units along the tethers, and therefore more efficiently convert the buoy's 3DoF motion into PTO work [14]-[16]. The two submerged PA variants can absorb 2-3 times more power than the single-tether generic PA in theory [12], [14], however, their engineering characteristics (e.g. optimal design maximising economic efficiency and PTO implementation) remain insufficiently explored for a commercialisation.

This paper conducts a comparison study between the three PA prototypes shown in Fig. 1, in order to better understand their dynamic response, power absorption efficiency, and optimal PTO design requirement, with an effort to provide insights into their engineering merits and economic viability relative to each other. The comparison is undertaken using numerical simulations based on the dynamic models of the PAs in the frequency-domain built upon linear wave theory. The layout of the paper is as follows: Section II describes the systems and their equations of motion, Section III discusses the simulation results and Section IV provides a summary of the results.

II. SYSTEM DESCRIPTION AND MOTION EQUATION

This study considers spherical buoys only for simplicity, particularly for the ease of analysis on a buoy with asymmetric mass distribution as shown in Fig. 2. In order to exclude uncertainties associated with a specific PTO design, it is presumed that the machinery force has linear spring and damper effects proportional to the tether elongation and the rate of change of the tether elongation, respectively. The tether stiffness is assumed to be at least two orders of magnitude higher than the PTO spring stiffness and therefore is regarded as a rigid component in the system. Linear wave theory is used to model the hydrodynamics of the PAs [9], and only monochromatic plane waves are considered. Therefore, the dynamics of the PAs can be simplified to a planar case of 3DoF motion and investigated in the frequency-domain.

A. Equation of Motion for Submerged Point Absorber

An oscillating body excited by a plane incident wave can be modelled based on the Cummins equation [17]:

$$(\mathbf{M} + \mathbf{A}_\infty)\ddot{\mathbf{x}} + \int_0^t \mathbf{K}_{rad}(t - \tau)\dot{\mathbf{x}}(\tau)d\tau = \mathbf{F}_{h/stat} + \mathbf{F}_d + \mathbf{F}_{exc} + \mathbf{F}_{pto}, \quad (1)$$

where the vector \mathbf{x} contains the surge displacement x , heave displacement z and pitch angle θ of the body at its geometrical centre; \mathbf{M} is the mass matrix of the oscillating body; \mathbf{A}_∞ is the hydrodynamic added mass existing at infinite frequency; $\mathbf{K}_{rad}(t)$ is the radiation impulse response function; and $\mathbf{F}_{h/stat}$, \mathbf{F}_d , \mathbf{F}_{exc} , and \mathbf{F}_{pto} are the hydrostatic, viscous drag, wave

excitation and PTO forces exerted on the body in Cartesian space, respectively.

As the buoy is fully submerged, the generalised hydrostatic force is

$$\mathbf{F}_{h/stat} = [0 \quad (\rho V - m)g \quad 0]^T, \quad (2)$$

where ρ is the density of water, m and V are the mass and volume of the buoy respectively, and g is the gravitational acceleration.

The viscous drag forces experienced by the buoy can be written as quadratic functions of the buoy velocity, based on the Morison equation [18]:

$$\mathbf{F}_d = \begin{pmatrix} -0.5\rho C_{Dx}A_x|\dot{x}|\dot{x} \\ -0.5\rho C_{Dz}A_z|\dot{z}|\dot{z} \\ -0.5\rho C_{D\theta}D^4D|\dot{\theta}|\dot{\theta} \end{pmatrix}, \quad (3)$$

where C_{Dx} , C_{Dz} , and $C_{D\theta}$ are the viscous drag coefficients of the buoy along surge, heave and pitch axes respectively, whose values can be found from [19] for various buoy shapes; A_x and A_z are the cross sectional areas of the buoy along surge and heave axes respectively; D is the diameter of the buoy. For the spherical buoy, $C_{Dx} = C_{Dz}$; $C_{D\theta} = 0$; and $A_x = A_z = \pi r^2$, where r is the radius of the buoy.

The PTO force exerted on the body is given by

$$\mathbf{F}_{pto} = \mathbf{J}(\mathbf{x})^{-T}\mathbf{F}_t, \quad (4)$$

where $\mathbf{J}(\mathbf{x})^{-T}$ is the transpose of an inverse Jacobian matrix \mathbf{J}^{-1} that relates the PTO force in the joint space \mathbf{F}_t (along the tether/s) to the PTO force in the task space \mathbf{F}_{pto} (along the buoy Cartesian coordinates), and is dependent on buoy position. \mathbf{F}_t consists of a static pretension force that overcomes the buoy's hydrostatic force; a spring force proportional to the tether elongation; and a damping force proportional to the rate of change of tether elongation. The forms of \mathbf{J}^{-1} and \mathbf{F}_t are dependent on the specific PA design and will be discussed in more details for each of the PA candidates in later subsections.

Assuming small displacements of the buoy with respect to the tether length, Equation (1) can be linearised at the nominal/rest position of the buoy, $\mathbf{x}_0 = [0 \quad 0 \quad 0]^T$, and thus can be written in the following frequency-domain form [10]:

$$(\mathbf{M} + \mathbf{A}(\omega))\hat{\mathbf{x}} + (\mathbf{B}_{rad}(\omega) + \mathbf{B}_a(\omega) + \mathbf{B}_{pto})\hat{\mathbf{x}} + \mathbf{K}_{pto}\hat{\mathbf{x}} = \hat{\mathbf{F}}_{exc}(\omega). \quad (5)$$

For a spherical buoy,

$$\mathbf{A}(\omega) = \begin{pmatrix} a_{11}(\omega) & 0 & 0 \\ 0 & a_{33}(\omega) & 0 \\ 0 & 0 & 0 \end{pmatrix},$$

$$\mathbf{B}_{rad}(\omega) = \begin{pmatrix} b_{11}(\omega) & 0 & 0 \\ 0 & b_{33}(\omega) & 0 \\ 0 & 0 & 0 \end{pmatrix},$$

$$\mathbf{B}_a(\omega) = \begin{pmatrix} b_s(\omega) & 0 & 0 \\ 0 & b_h(\omega) & 0 \\ 0 & 0 & 0 \end{pmatrix},$$

$$\hat{\mathbf{F}}_{exc}(\omega) = \begin{pmatrix} \hat{F}_s(\omega) \\ \hat{F}_h(\omega) \\ 0 \end{pmatrix}, \quad (6)$$

where a_{ii} and b_{ii} denote the frequency-dependent hydrodynamic coefficients (added mass and radiation damping respectively) of the buoy at its rest position; b_s and b_h are the frequency and buoy velocity dependent viscous damping

coefficients along surge and heave axes respectively, which are approximated from Equation (3) using Lorentz linearisation [20]; \hat{F}_s and \hat{F}_h represent the wave excitation force along surge and heave axes of the buoy. The superscript $\hat{\cdot}$ denotes the complex amplitudes. The hydrodynamic coefficients and the wave excitation forces can be calculated using boundary element solvers such as WAMIT, AQWA and NEMOH for any buoy shapes. For submerged spherical buoys, a_{ii} , b_{ii} , \hat{F}_s and \hat{F}_h can be calculated using an analytical method described in [21]. \mathbf{M} , \mathbf{B}_{pto} , and \mathbf{K}_{pto} in Equation (5) are dependent on the specific PA design and thus will be discussed in the later subsection for each PA candidate. The hydrostatic force disappears in Equation (5) as it is cancelled by the PTO pretension force.

B. Generic Single Tether Point Absorber

For the generic single tether PA design shown in Fig. 1(a), the PTO force along the tether is

$$F_t = C_{pto} - B_{pto}\Delta\dot{l} - K_{pto}\Delta l, \quad (7)$$

where $C_{pto} = -(\rho V - m)g$ is a pretension (offset) force that counteracts the buoyancy/hydrostatic force along the z-axis; B_{pto} and K_{pto} are the PTO stiffness and damping respectively; Δl is the tether/PTO elongation. The inverse Jacobian matrix of the system \mathbf{J}^{-1} is described in [11] and is not repeated here.

Applying linearisation to the PA system at its nominal/rest position (for more details about the linearisation procedure, please refer to [16]), the following mass and PTO damping and stiffness matrices associated with Equation (5) are obtained:

$$\mathbf{M} = \begin{pmatrix} m & 0 & 0 \\ 0 & m & 0 \\ 0 & 0 & I_{yy} \end{pmatrix},$$

$$\mathbf{B}_{pto} = \begin{pmatrix} 0 & 0 & 0 \\ 0 & B_{pto} & 0 \\ 0 & 0 & 0 \end{pmatrix},$$

$$\mathbf{K}_{pto} = \begin{pmatrix} -C_{pto}/l_0 & 0 & C_{pto}r/l_0 \\ 0 & K_{pto} & 0 \\ C_{pto}r/l_0 & 0 & -C_{pto}r(l_0 + r)/l_0 \end{pmatrix}, \quad (8)$$

where I_{yy} is the moment of inertia of the buoy about the pitch (y) axis; r and l_0 denote the radius of the spherical buoy and the nominal tether length at the rest pose of the buoy respectively. Equation (8) shows that the PTO control is directly applied to the heave mode only.

At the nominal position of the buoy, the elongation velocity of the tether/PTO is given by

$$\Delta\dot{l} = \mathbf{J}(\mathbf{x}_o)^{-1}\hat{\mathbf{x}} = (0 \quad 1 \quad 0)\hat{\mathbf{x}}, \quad (9)$$

where $\mathbf{J}(\mathbf{x}_o)^{-1}$ is the inverse Jacobian matrix at the buoy nominal position. The time-averaged absorbed power by the system is then equal to the mechanical power dissipated by the linear PTO damper on the tether:

$$P_a = \frac{1}{2}B_{pto}|\Delta\dot{l}|^2. \quad (10)$$

C. Asymmetric Mass Distribution Point Absorber

The purpose of having an asymmetric mass distribution (AMD) PA as shown in Fig. 1(b) is to enhance dynamic coupling between the oscillating modes of the buoy, with the aim to increase power absorption by the surge mode.

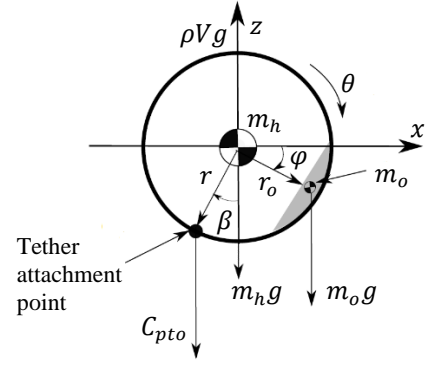


Fig. 2 Schematic showing the x-z plane of a spherical buoy with asymmetric mass distribution at its rest position.

Fig. 2 shows a cross section view of a spherical buoy with asymmetric mass distribution, on the x-z plane that the buoy is symmetric about. A body-fixed coordinate frame is located at the geometric centre of the buoy. The buoy consists of a spherical hull with a radius r and a mass m_h , and an additional mass m_o offset from the geometric centre of the buoy, resulting in an eccentric buoy centre of gravity on the x-z plane. The location of m_o on the x-z plane is defined by the offset distance r_o and the offset angle φ with respect to the positive x-axis. For the buoy to remain at rest in calm water, the PTO pretension (offset) force is given by

$$C_{pto} = -(\rho V - m_h - m_o)g. \quad (11)$$

In addition, in order to balance the torque generated by the offset mass about the geometric centre of the buoy, the tether attachment point is rotated clockwise around the surface of the hull on the x-z plane. The line passing through the geometric centre of buoy and the tether attachment point forms an angle β with respect to the negative z-axis, which can be calculated by solving

$$C_{pto} \cdot r \sin(\beta) = m_o g \cdot r_o \cos(\varphi). \quad (12)$$

A similar linearisation procedure is applied to the AMD PA, as detailed in [16]. The resulting mass, PTO damping and stiffness matrices associated with Equation (5) are given by:

$$\mathbf{M} = \begin{pmatrix} m_h + m_o & 0 & -m_o r_o \sin(\varphi) \\ 0 & m_h + m_o & -m_o r_o \cos(\varphi) \\ -m_o r_o \sin(\varphi) & -m_o r_o \cos(\varphi) & I_{yy,o} \end{pmatrix},$$

$$\mathbf{B}_{pto} = \begin{pmatrix} 0 & 0 & 0 \\ 0 & B_{pto} & B_{pto}r \sin(\beta) \\ 0 & B_{pto}r \sin(\beta) & B_{pto}r^2 \sin^2(\beta) \end{pmatrix},$$

$$\mathbf{K}_{pto} = \begin{pmatrix} -C_{pto}/l_0 & 0 & C_{pto}r \cos(\beta)/l_0 \\ 0 & K_{pto} & K_{pto}r \sin(\beta) \\ C_{pto}r \cos(\beta)/l_0 & K_{pto}r \sin(\beta) & \begin{pmatrix} -C_{pto}r \cos(\beta)(l_0 + r \cos(\beta))/l_0 \\ -m_o g r_o \sin(\varphi) + K_{pto}r^2 \sin^2(\beta) \end{pmatrix} \end{pmatrix} \quad (13)$$

Compared with the same matrices for the generic case in Equation (8), \mathbf{M} , \mathbf{B}_{pto} , and \mathbf{K}_{pto} in Equation (13) exhibit additional couplings (e.g. heave-pitch and surge-pitch) due to the asymmetric mass distribution.

At the nominal position of the buoy (as shown in Fig. 2), the elongation velocity of the tether/PTO is given by

$$\Delta \hat{l} = \mathbf{J}(\mathbf{x}_o)^{-1} \hat{\mathbf{x}} = \begin{pmatrix} 0 & 1 & r \sin(\beta) \end{pmatrix} \hat{\mathbf{x}}. \quad (14)$$

The inverse Jacobian matrix shows that both the heave and pitch modes directly couple to the tether/PTO elongation. The time-averaged absorbed power of the asymmetric mass distribution system is also given by Equation (10).

D. Three Tether Point Absorber

The purpose of having the three-tether PTO arrangement is to enhance kinematic coupling between the oscillating modes of the buoy and the PTO units along the tethers, allowing more efficient conversion of the buoy 3DoF motion into PTO work.

Fig. 3 illustrates a schematic of a three-tether point absorber at its rest pose, where the tethers are equally distributed around the buoy, separated by 120° in the horizontal plane. This configuration makes the system insensitive to wave direction. Tether 1 aligns with the x-z plane, and thus the wave travelling direction, and tethers 2 and 3 are symmetric about the x-z plane. In this paper, it is assumed that all three tethers point towards the geometric centre of the spherical buoy and the PTO units along the three tethers have identical linear characteristics (e.g. pretension force, PTO damping and stiffness). The tether attachment points are located on the surface of the buoy hull. The inclination angle of the tethers with respect to the z-axis, α , plays an important role in this design as it defines the contribution of the surge and heave modes in the total absorbed power, as well as the effects of PTO control on the surge and heave modes. The PTO force along each tether is

$$F_{t,i} = C_{pto}/3 \cos(\alpha) - B_{pto} \Delta \hat{l}_i - K_{pto} \Delta l_i, \quad (15)$$

where $C_{pto}/3 \cos(\alpha)$ is the pretension (offset) force generated by the PTO unit on each tether. The three PTO units jointly provide a total pretension force C_{pto} along the z-axis that counteracts the buoyancy/hydrostatic force of the buoy.

The three tether PA has a mass matrix identical to the generic single tether PA. Following the linearisation procedure reported in [14], the PTO damping and stiffness matrices for the three tether PA can be derived as shown in Equation (16). Compared with the same matrices for the single tether case in Equations (8) and (13), \mathbf{B}_{pto} and \mathbf{K}_{pto} in Equation (16) demonstrate additional PTO control directly applied to the surge mode, enabled by inclining the tether by α .

$$\mathbf{B}_{pto} = \begin{pmatrix} \frac{3}{2} B_{pto} \sin^2(\alpha) & 0 & 0 \\ 0 & 3 B_{pto} \cos^2(\alpha) & 0 \\ 0 & 0 & 0 \end{pmatrix}, \quad (16)$$

$$\mathbf{K}_{pto} = \begin{pmatrix} \left(\frac{3}{2} \sin^2(\alpha) \left(K_{pto} + \frac{C_{pto}}{3 l_0 \cos(\alpha)} \right) \right) & 0 & C_{pto} r / l_0 \\ -\frac{C_{pto}}{l_0 \cos(\alpha)} & 0 & 0 \\ 0 & \left(3 \cos^2(\alpha) \left(K_{pto} + \frac{C_{pto}}{3 l_0 \cos(\alpha)} \right) \right) & 0 \\ C_{pto} r / l_0 & 0 & \frac{-C_{pto} r (l_0 + r) (\cos^2(\alpha) + 1)}{2 l_0 \cos(\alpha)} \end{pmatrix}.$$

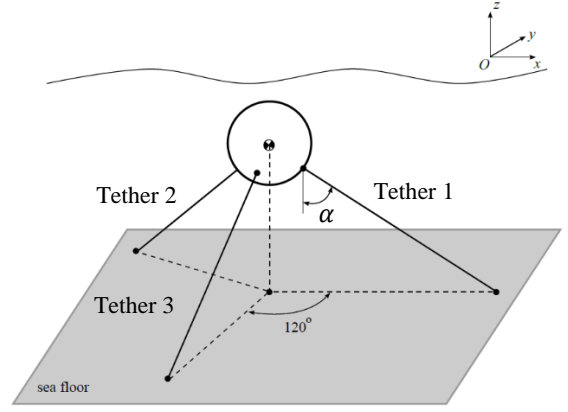


Fig. 3 Schematic showing a three-tether point absorber with a submerged spherical buoy at its rest pose

At the nominal position of the buoy (as shown in Fig. 3), the elongation velocities of the tethers/PTOs are given by

$$\Delta \hat{l} = \begin{pmatrix} \Delta \hat{l}_1 \\ \Delta \hat{l}_2 \\ \Delta \hat{l}_3 \end{pmatrix} = \mathbf{J}(\mathbf{x}_o)^{-1} \hat{\mathbf{x}} = \begin{pmatrix} -\sin(\alpha) & \cos(\alpha) & 0 \\ \sin(\alpha)/2 & \cos(\alpha) & 0 \\ \sin(\alpha)/2 & \cos(\alpha) & 0 \end{pmatrix} \hat{\mathbf{x}}. \quad (17)$$

The inverse Jacobian matrix shows that both the surge and heave modes directly couple to the tether/PTO elongations. The time-averaged absorbed power is equal to the mechanical power dissipated by the three PTO units:

$$P_a = \sum_{i=1}^3 \frac{1}{2} B_{pto} |\Delta \hat{l}_i|^2. \quad (18)$$

E. Power Absorption and Optimal Condition

The time-averaged absorbed power can also be calculated in the Cartesian coordinates as the difference between the wave power input into the system and the power radiated and dissipated in water [6]:

$$P_a = \frac{1}{4} (\hat{\mathbf{F}}_{exc}^* \hat{\mathbf{x}} + \hat{\mathbf{x}}^* \hat{\mathbf{F}}_{exc}) - \frac{1}{2} \hat{\mathbf{x}}^* (\mathbf{B}_{rad} + \mathbf{B}_d) \hat{\mathbf{x}}, \quad (19)$$

where $*$ denotes the conjugate transpose. Furthermore, the total absorbed power can be decomposed into power absorption by the surge and heave modes respectively:

$$P_{a,s} = \frac{1}{4} (\hat{F}_s^* \hat{x} + \hat{x}^* \hat{F}_s) - \frac{1}{2} \hat{x}^* (b_{11} + b_s) \hat{x},$$

$$P_{a,h} = \frac{1}{4} (\hat{F}_h^* \hat{z} + \hat{z}^* \hat{F}_h) - \frac{1}{2} \hat{z}^* (b_{33} + b_h) \hat{z}. \quad (20)$$

For a spherical buoy, there is neither excitation torque nor hydrodynamic damping on its rotational axis. Therefore, the power absorption from the pitch mode of the buoy is zero.

Maximum power is absorbed when the velocity of the buoy is unconstrained and equal to:

$$\hat{\mathbf{x}}_{opt} = \frac{1}{2}(\mathbf{B}_{rad} + \mathbf{B}_d)^{-1}\hat{\mathbf{F}}_{exc}, \quad (21)$$

which is the optimal velocity. Equation (21) shows that the buoy optimal velocity is in phase with the excitation force and of optimal amplitude scaled by the damping coefficients [8]. The maximum power available in the surge and heave modes by an axisymmetric body in monochromatic waves are:

$$\begin{aligned} P_{a,s}^{rad} &= 2J_t/k, \\ P_{a,h}^{rad} &= J_t/k, \end{aligned} \quad (22)$$

where J_t denotes the power transport per unit width of the wave frontage and k denotes the wavenumber [8]. The superscript *rad* denotes the power limit of the mode governed by the radiation ability of the mode oscillating at the optimal velocity.

The relative capture width (RCW) is a measure of the efficiency of the WEC device with respect to its size and is given by

$$RCW = P_a/(2rJ_t). \quad (23)$$

F. Optimisation of Absorbed Power

In order to have a fair comparison of the power absorption capability of the three PAs, it is assumed that all PAs have the same size of buoy and physical constraints, and are located at the same submergence depth but operate under their own optimal PTO configurations, which are wave frequency dependent. Therefore, the optimisation goal is to maximise P_a subject to constraints by seeking the frequency-dependent optimal \mathbf{B}_{pto} and \mathbf{K}_{pto} matrices.

For the single tether PAs, \mathbf{B}_{pto} and \mathbf{K}_{pto} are governed by K_{pto} , B_{pto} , l_0 , and C_{pto} , where C_{pto} is set to overcome the hydrostatic force and thus is a fixed value, whilst the other three PTO parameters can be tuned to achieve optimality. l_0 can be physically changed increasing the height of the mooring above the ocean floor, however, a discussion on how specific designs impact on hydrodynamics, and resulting economic viability is out of the scope of the current paper. Substituting Equations (6), (8) and (13) into Equation (5), ignoring all the off-diagonal/coupling terms and comparing with Equation (21), the theoretical optimal values of K_{pto} , B_{pto} and l_0 can be found for the single tether PAs:

$$\begin{aligned} K_{pto,t} &= (m + a_{33}(\omega))\omega^2, \\ B_{pto,t} &= b_{33}(\omega) + b_h(\omega), \\ l_{0,t} &= C_{pto}/[(m + a_{11}(\omega))\omega^2], \end{aligned} \quad (24)$$

where $K_{pto,t}$ and $B_{pto,t}$ achieve the optimal phase (resonance) and amplitude conditions for the decoupled heave mode; $l_{0,t}$ achieves the resonance condition for the decoupled surge mode, implying that for small buoy displacements the surge mode of the bottom-referenced single tether PA is analogous to an inverted pendulum. The theoretical optimal values in Equation (24) do not represent the real optimal values for the systems because dynamic coupling is ignored and physical constraints are not considered. However, they can be used as an initial guess for the PTO optimisation. The optimisation goal for the single tether PAs is then

$$\max\{P_a(K_{pto}, B_{pto}, l_0)\}, \quad (25)$$

subject to the nominal tether length constraint $l_{0,min} \leq l_0 \leq l_{0,max}$ and the tether elongation (PTO stroke) constraint $|\Delta\hat{l}| \leq \Delta l_{max}$.

For the three tether system, \mathbf{B}_{pto} and \mathbf{K}_{pto} are predominantly governed by K_{pto} , B_{pto} , and α . l_0 is determined from the inverse kinematics of the system assuming the tethers are anchored at the sea floor as shown in Figure 3. The optimisation goal for the three tether PA is then

$$\max\{P_a(K_{pto}, B_{pto}, \alpha)\}, \quad (26)$$

subjected to the tether inclination angle constraint $0 \leq \alpha \leq 90^\circ$ and the PTO stroke constraint $|\Delta\hat{l}| \leq \Delta l_{max}$. The initial value of α for optimisation is set to 55° based on the results in [9]. The initial values of K_{pto} and B_{pto} can be obtained from the following equations given known C_{pto} , α , and l_0 :

$$\begin{aligned} \frac{3}{2}\sin^2(\alpha)\left(K_{pto,t} - \frac{C_{pto}}{3l_0\cos(\alpha)}\right) + \frac{C_{pto}}{l_0\cos(\alpha)} &= (m + a_{11}(\omega))\omega^2, \\ B_{pto,t} &= 2(b_{11}(\omega) + b_s(\omega))/3\sin^2(\alpha_a), \end{aligned} \quad (27)$$

which respectively satisfy the optimal phase and amplitude conditions for the decoupled surge mode. We take the priority to tune the system to be optimal in the surge mode because it contains twice power compared to the heave mode for unconstrained buoy motion as shown in Equation (22). Optimisation is implemented using the *fmincon* command in MATLAB Optimisation Toolbox.

G. System Parameters for Simulation

Simulation parameters are listed in Table 1. The buoys for the three PAs are assumed to have the same geometrical shape (sphere), size (radius), and weight (total mass), and are submerged at the same water and submergence depth. The buoy with asymmetric mass distribution has identical hull mass and offset mass, with the offset mass located at a near-optimal location [16]. The buoy hull is assumed to be hollow so that PTO circuits and control instruments can be placed inside. For the single tether PAs, their nominal tether length is constrained between 5m and 50m in optimisation, defined to ensure the fidelity of the optimisation results without taking the feasibility of the specific design into consideration. Maximum PTO stroke of 3m is applied to all systems to prevent the buoy from breaking the water surface, and thus to constrain the problem within the boundaries of linear wave theory. Simulations were run across frequencies between 0.3 and 1.6 rad/s. By default, 0.1m wave amplitude is used unless otherwise stated. PTO optimisation is conducted at each wave frequency for the three PAs, following the procedures discussed in Section II.F.

TABLE I SYSTEM PARAMETERS FOR SIMULATION

Symbol	Value/unit	Description
d_w	50m	Water depth of the sea
h_s	8.5m	Submergence depth from buoy geometric centre to water surface
r	5m	Radius of the spherical buoy
m	2.68×10^5 kg	Buoy mass, defined as half of the buoy buoyancy force $m = \rho V/2$

m_h	$1.34 \times 10^5 \text{kg}$	Hull mass for the buoy with asymmetric mass distribution
m_o	$1.34 \times 10^5 \text{kg}$	Offset mass for the buoy with asymmetric mass distribution
r_o	4m	Offset distance of the offset mass m_o
φ	30°	Offset angle of the offset mass m_o
I_{yy}	$4.472 \times 10^6 \text{kg} \cdot \text{m}^2$	Moment of inertia of a hollow spherical buoy about its pitch axis, given by $I_{yy} = \frac{2}{3}mr^2$
$I_{yy,o}$	$4.383 \times 10^6 \text{kg} \cdot \text{m}^2$	Moment of inertia of a hollow spherical buoy with offset mass about its pitch axis, given by $I_{yy,o} = \frac{2}{3}m_h r^2 + m_o r_o^2$
$l_{0,min}$, $l_{0,max}$	5m, 50m	Nominal tether length limits for the single tether systems
Δl_{max}	3m	Tether elongation constraint (PTO maximum stroke)
ω	0.3-1.6rad/s	Wave frequency range (regular)
A_w	0.1m	Wave amplitude (regular)

III. RESULTS

This section presents and discusses results categorised into six main aspects that are critical from an engineering perspective: optimal PTO parameters, dynamic response, power absorption, PTO force, power to PTO force ratio, and bandwidth. For convenience, the generic single tether PA, the asymmetric mass distribution PA, and the three tether PA are abbreviated as the *GIT*, the *AMD* and the *3T* respectively.

A. Optimal PTO Parameters

A comparison of the frequency-dependent optimal PTO parameters for the three PAs is shown in Fig. 4. With regard to

the *GIT*, its optimised nominal tether length fluctuates randomly between the defined limits across the wave frequencies (not displayed in the figure) which implies that its power absorption does not depend on the surge (inverted pendulum) mode. This outcome is expected for the *GIT* given there is no coupling between its surge mode and tether/PTO elongation as evident in Equations (8) and (9). Therefore, the nominal tether length of the *GIT* is fixed to $d_w - h_s - r = 36.5\text{m}$ across the wave frequencies, assuming the tether is anchored to the sea floor level and requires no tower. For the *AMD*, the optimal nominal tether length decreases sharply with an increase in wave frequency and reaches the lower limit at 0.72rad/s . By comparison, the *3T* has its optimal tether inclination angle barely varying across the wave frequencies.

The *GIT* and the *3T* have similar optimal PTO stiffness and damping that smoothly increase across the wave frequencies. The optimal stiffness and damping of the *3T* are generally lower than the that of the *GIT*. In contrast, the *AMD* demonstrates much larger variations in its optimal PTO stiffness and damping across the wave frequencies, which indicates more challenges in its PTO design and manufacture. The optimal stiffness of the *AMD* is lower than the optimal stiffness of the *GIT* for low to medium frequency waves but is higher for high frequency waves. The optimal damping of the *AMD* is dramatically higher than the optimal damping of the *GIT*, in particular for low to medium frequency waves, where a peak difference of over one order of magnitude is observed. In the following subsections, results are presented for the PA candidates that operate under the frequency-dependent optimal PTO parameters as shown in Fig. 4, unless otherwise explicitly stated.

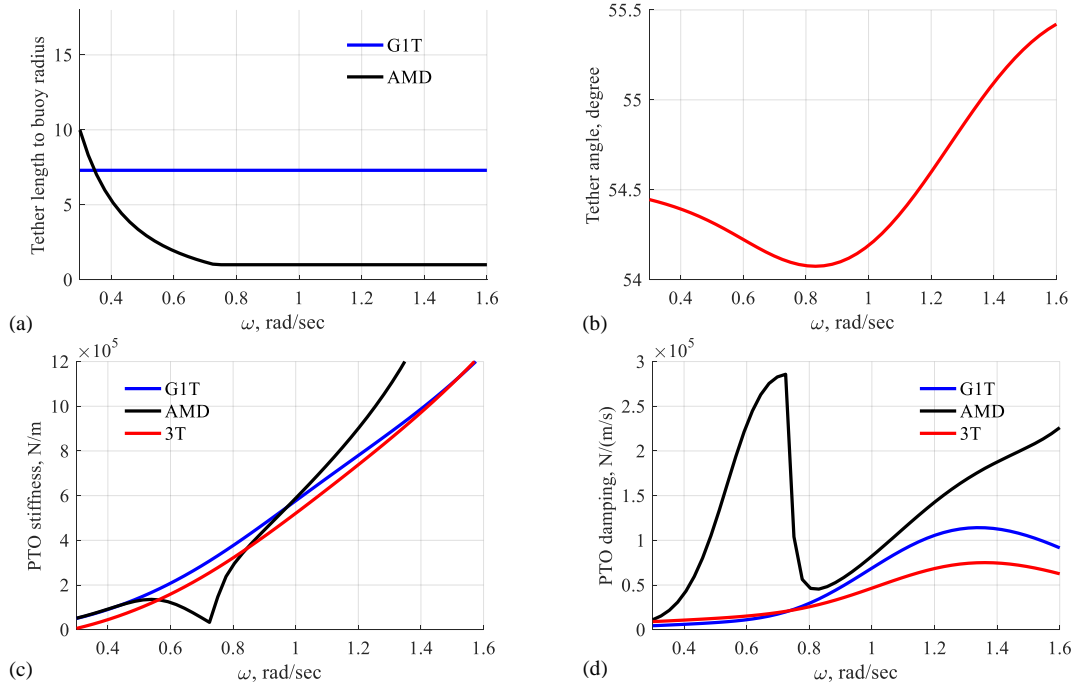


Fig. 4 Comparison of the frequency-dependent optimal PTO parameters for the three PAs: (a) optimal nominal tether length l_0 normalised by buoy radius for the *GIT* and the *AMD*; (b) optimal tether inclination angle for the *3T*; (c) optimal PTO stiffness K_{pto} ; (d) optimal PTO damping B_{pto} .

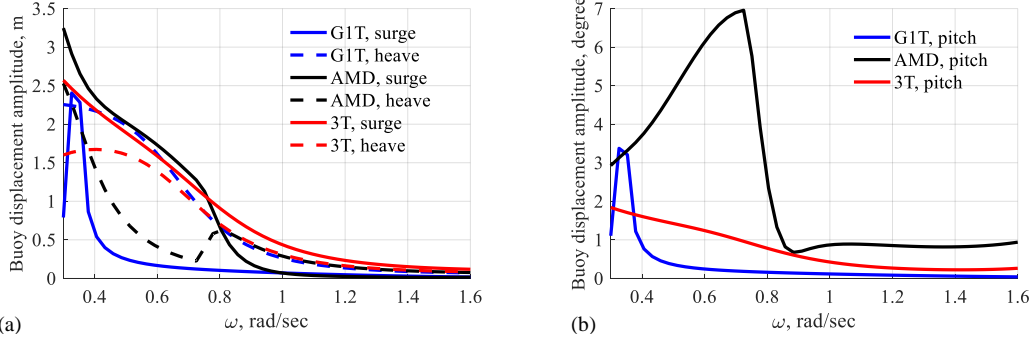


Fig. 5 Comparison of the buoy displacement amplitudes for the three PAs $|\hat{\mathbf{x}}|$ under their optimal PTO configurations: (a) surge displacement $|\hat{x}|$ and heave displacement $|\hat{z}|$; (b) pitch displacement $|\hat{\theta}|$.

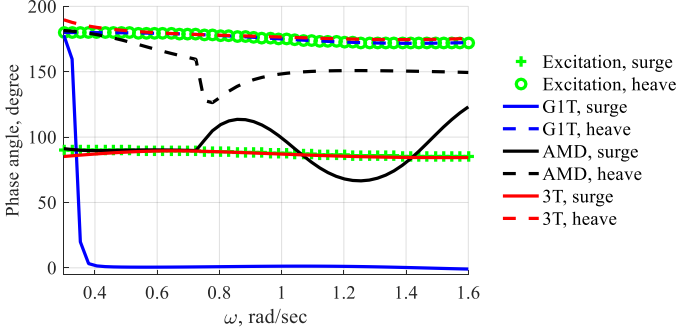


Fig. 6 Comparison between the buoy velocity phases $\angle \dot{\hat{\mathbf{x}}}$ for the three PAs and the excitation force phases $\angle \hat{\mathbf{F}}_{exc}$

B. Dynamic Response

A comparison of the buoy displacement amplitudes for the three PAs is shown in Fig. 5, while a comparison between the buoy velocity phases for the three PAs and the excitation force phases is shown in Fig. 6.

As was shown in the last subsection, the G1T can only absorb power from heave. Thus, the G1T has the buoy heave velocity in phase with the heave excitation force across the wave frequencies, indicating the buoy heave response reaches its resonance or optimal phase condition as shown in Equation (21), resulting in relatively large heave displacement across the wave frequencies. In contrast, the buoy surge velocity and the surge excitation force are only in phase at a single frequency of 0.3rad/s, and are almost 90° out of phase at other wave frequencies, resulting in a resonance peak at 0.3rad/s in the surge displacement. This is due to the fact that the nominal tether length of the G1T (that governs the surge natural frequency) is fixed across the wave frequencies. The resonance peak in the surge response also induces a peak in the pitch response via the surge-pitch coupling as shown by the stiffness matrix in Equation (8).

In comparison to the G1T, the 3T has both its surge and heave modes tuned to resonance across the wave frequencies, as evident in Fig. 6, where both its buoy surge and heave velocities are in phase with the surge and heave excitation forces across the wave frequencies. This results in relatively large surge and heave displacements across the frequencies. In contrast, the pitch response of the 3T is relatively small across the wave frequencies stabilised by the 3T configuration.

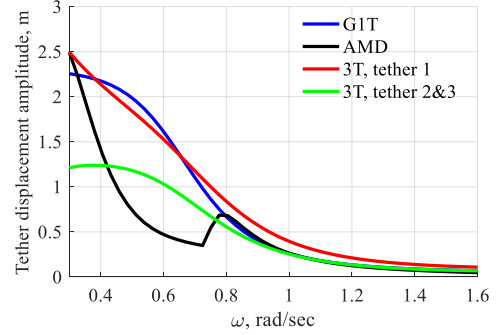


Fig. 7 Comparison of the tether elongation displacement amplitudes $|\Delta \hat{l}_i|$

The AMD performance lies between the G1T and the 3T, and its surge and heave modes can only both be tuned to resonance for low frequency waves (below 0.45rad/s), where both the surge and heave displacements are relatively large. Between 0.45rad/s and 0.72rad/s, optimisation tunes the surge mode of the AMD in resonance as the surge mode contains more power than the heave mode. Thus, surge displacement is much larger than the heave displacement in this frequency range. Above 0.72rad/s, the surge (inverted pendulum) mode of the AMD can no longer be tuned to resonance because the nominal tether length reaches the lower limit. As a result, optimisation evaluates the available power in the surge mode and the heave mode to determine their contributions. An intersection between the surge and heave displacement curves at 0.8rad/s indicates that the AMD switches to extract more power from the heave mode. In comparison to the G1T and the 3T, the AMD has higher pitch response below 0.72rad/s because the AMD converts power from its surge mode into PTO work via surge-pitch and heave-pitch couplings as indicated by Equation (13).

A comparison of the amplitudes of tether elongation displacements is shown in Fig. 7. For the G1T and the AMD, their tether elongation displacements are almost identical to the buoy heave displacements, due to their inverse kinematics at the nominal position of the buoy. The 3T has its first tether oscillating with amplitudes similar as that of the G1T, and its second and third tethers oscillating with amplitudes about two thirds that of the first tether. The AMD requires much less tether elongation than either the G1T or the 3T to absorb maximum power for low to medium frequency waves.

C. Power Absorption

A comparison of the RCWs of the three PAs is shown in Fig. 8. Also shown is the theoretical RCW limits of the heave mode and the combined surge and heave mode. The high frequency RCW limits are defined by the radiation ability of the buoy when operating at optimal velocity given unconstrained motion, calculated from Equations (22) and (23):

$$RCW_s^{rad} = 2RCW_h^{rad} = 1/(kr) \quad (28)$$

where the subscripts s and h denote the surge mode and the heave mode respectively. The low frequency RCW limits are defined by the maximum swept volume (MSV) of the buoy, given by the following equation for a submerged sphere:

$$RCW_s^{msv} = RCW_h^{msv} = \rho e^{-kh_s} d_{max} V A_w \omega^3 / (2rJ_t) \quad (29)$$

where d_{max} denotes the maximum buoy displacement of the corresponding mode [9], and is set as 3m for both the heave mode and the surge mode to be consistent with the tether elongation constraint defined in optimisation.

The G1T has the lowest RCW among the three PAs and converges to the RCW_h^{rad} curve at high frequencies. The 3T has the highest RCW among the three PAs (2-3 times that of the G1T) that converges to the $RCW_s^{rad} + RCW_h^{rad}$ curve at high frequencies. The AMD performs between the G1T and the 3T, and has its RCW converge to the 3T curve at low frequencies and to the G1T curve at high frequencies. At low frequencies, the RCWs of the PAs are lower than the RCW_h^{msv} curve and the $RCW_s^{msv} + RCW_h^{msv}$ curve. This is because the calculations of the RCW^{msv} limits do not consider the effects of viscous loss. The linearised viscous damping is significantly higher than the radiation damping at low wave frequencies as shown in Fig. 9, which dissipates additional energy in water.

The RCW of each PA is decomposed into the RCWs of the surge mode and the heave mode using Equation (20), with results demonstrated in Fig. 10. The G1T purely absorbs power from its heave mode across the wave frequencies as expected. The 3T absorbs the same amount of power as the G1T from its heave mode and absorbs up to twice the power from its surge mode at high frequencies. The power absorbed by the surge mode and the heave mode of 3T are similar at low frequencies because the surge mode experiences more viscous losses than the heave mode, as shown in Fig. 9. The AMD exhibits power absorption behaviour matching its dynamic response behaviour shown in Fig. 6. For wave frequencies below 0.45rad/s, the power absorbed by the modes of the AMD are equal to those of the 3T. Between 0.45rad/s and 0.72rad/s, the power absorbed by the surge mode of the AMD is equal to that of the 3T, whilst the power absorbed by the heave mode of the AMD is less than that of the 3T. Above 0.72rad/s when the nominal tether length reaches the lower limit, the AMD decreases power absorption from its surge mode and increases power absorption from its heave mode with an increase in wave frequency, and trends towards the G1T at high frequencies.

The power absorption capabilities of the 3T and the AMD are compared under various wave amplitudes but subject to the same tether elongation constraint of 3m, with the q-factors denoting the ratio of the absorbed power by the 3T to the absorbed power by the AMD as shown in Fig. 11. In general, the 3T absorbs more power than the AMD, in particular for very

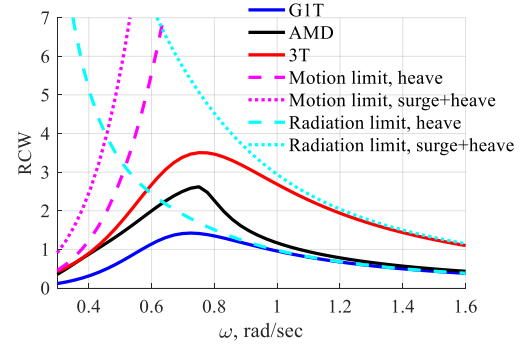


Fig. 8 Comparison of the RCWs of the three PAs (solid lines) and the RCW limits of the heave mode (dashed lines) and the combined surge and heave modes (dotted lines). The RCW limits in magenta and cyan are respectively defined by the maximum swept volume of the buoy and the radiation ability of the buoy given unconstrained motion.

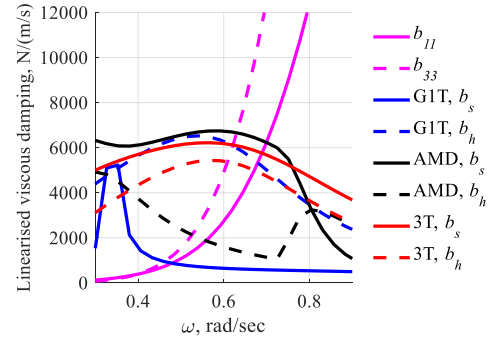


Fig. 9 Comparison of the radiation damping coefficients b_{11} and b_{33} and the linearised viscous damping coefficients b_s and b_h for the three PAs.

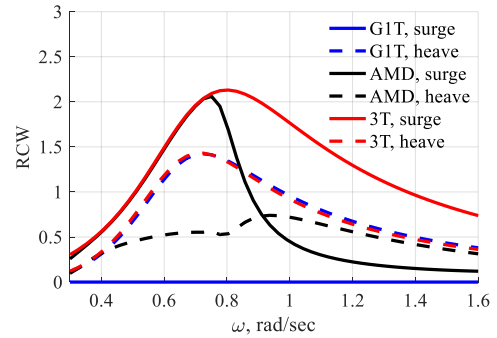


Fig. 10 Comparison of the RCWs associated with the individual modes.

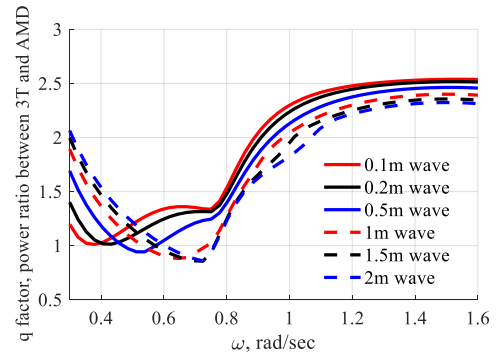


Fig. 11 Comparison of the q factors as an efficiency improvement ratio between power absorption from the 3T and the AMD for various wave amplitudes.

low and high frequency waves. For medium frequency waves, the q-factor decreases with an increase in wave amplitude, to less than unity. This is due to the fact that the 3T requires more tether elongation displacement than the AMD to absorb maximum power from medium frequency waves as evident in Fig. 7. Thus, excited by large waves, the 3T is more likely to reach its tether elongation constraint compared to the AMD.

D. PTO Force

A comparison of the dynamic PTO forces and the net PTO forces for the three PAs are shown in Fig. 12 and Fig. 13 respectively. The dynamic PTO force of the AMD is two to four times lower than that of the G1T at medium wave frequencies between 0.45rad/s and 0.72rad/s. This is because in this frequency range the AMD has lower optimal PTO stiffness and lower tether elongation displacement than those of the G1T, which leads to a significantly lower stiffness force. The average of the dynamic PTO forces on the tethers of the 3T is two to four times lower than the dynamic PTO force of the G1T at frequencies below 0.72rad/s. The dynamic PTO forces on the second and third tethers of the 3T are about two thirds of that on its first tether on average across the wave frequencies. For the three PAs, their net PTO forces are dominated by the pretension forces used to overcome the buoy buoyancy force when excited by small waves. The tethers of the 3T have a pretension force that is 60% of the pretension force of the G1T and the AMD due to the tripod formation of the 3T.

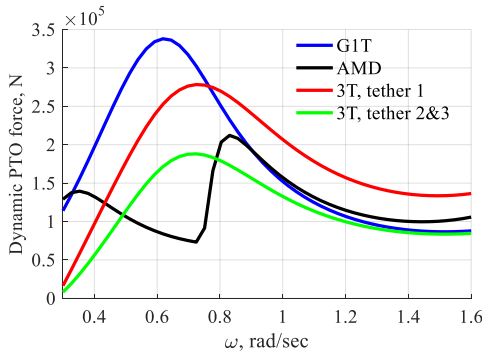


Fig. 12 Comparison of the dynamic (spring and damper) PTO forces

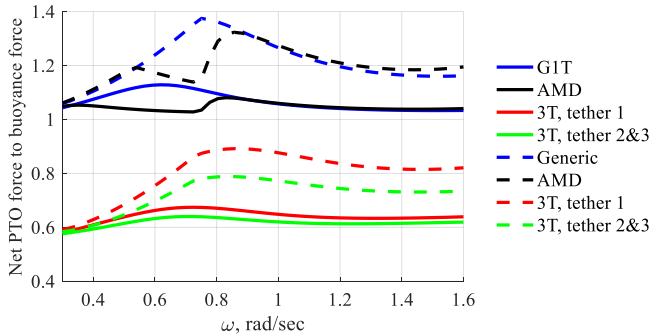


Fig. 13 Comparison of the net PTO force (sum of the PTO dynamic and pretension forces) normalised by the buoy buoyancy force. The solid lines denote results for 0.1m wave amplitude and the dashed lines denote results for 0.5m wave amplitude.

E. Power to PTO Force Ratio

The root mean square (RMS) of the net PTO force relates to the costs of the PTO and the mooring. Therefore, a cost-related performance index of power to PTO force ratio $P_a/F_{t,RMS}$ that indicates the cost of PTO and mooring facility per kW is used to assess the economic viability of the PAs. A comparison of this cost-related index is conducted for two wave amplitudes and across the wave frequencies, with the q-factors that correspond to the increase of $P_a/F_{t,RMS}$ between the PAs as shown in Fig. 14. The AMD has its power to PTO force ratio twofold that of the G1T for low to medium frequency waves that have high occurrence probability in most seas. For the 3T, its power to PTO force ratio is calculated in two ways for comparison: 1) the absorbed power divided by the RMS of the net PTO force on the first tether, assuming that the three tethers share a common PTO circuit and thus the RMS of the highest net PTO force among tethers indicates the whole PTO cost; 2) the absorbed power divided by the sum of the RMS of the net PTO forces on all tethers, assuming that the tethers employ uncoupled PTO units. When having uncoupled PTO units, the 3T has its power to PTO force ratio slightly higher than that of the G1T. However, if the desired PTO forces on the tethers can be achieved by a shared PTO circuit, the 3T has a power to PTO force ratio over three times higher than the G1T.

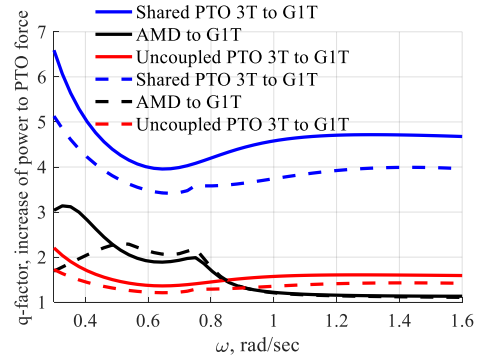


Fig. 14 Comparison of the q factors that correspond to the increase of the power to PTO force ratio between the PAs. The solid lines denote results for 0.1m wave amplitude and the dashed lines denote results for 0.5m wave amplitude.

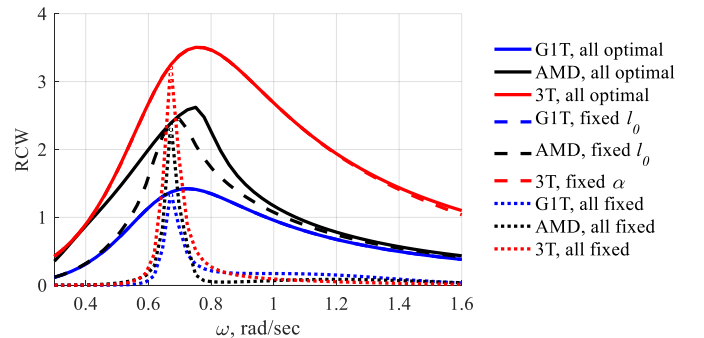


Fig. 15 Comparison of RCWs and bandwidths of the three PAs with: 1) fully optimal PTO parameters – frequency-dependent optimal K_{pto} , B_{pto} , l_0 or α (solid lines); 2) frequency-dependent optimal K_{pto} and B_{pto} but fixed l_0 or α only optimal at 0.67rad/s (dashed lines); 3) fully fixed PTO parameters – fixed K_{pto} , B_{pto} , l_0 or α only optimal at 0.67rad/s (dotted lines).

F. Absorption Bandwidth

Absorption bandwidth of the WEC corresponds to the frequency range where the absorbed power stays within 50% of its maximum value. It indicates the power absorption capability of the WEC in stochastic seas, where the wave frequency and amplitude vary continuously with time. Fig. 15 compares the absorption bandwidth of the three PAs operating with 1) frequency-dependent optimal PTO parameters (as used in the previous subsections); 2) frequency-dependent optimal PTO stiffness and damping but nominal tether length and tether inclination angle fixed to their optimal values for the 0.67rad/s wave; and 3) PTO parameters all fixed to their optimal values for the 0.67rad/s wave. 0.67rad/s (9.4s) wave was selected as it often occurs in sea. Fixing the nominal tether length and the tether inclination angle do not compromise the absorption bandwidth of the G1T or the 3T (about 0.7rad/s). In contrast, fixing the nominal tether length reduces the absorption bandwidth of the AMD from 0.45rad/s to 0.3rad/s. For all the PAs, their bandwidth is significantly reduced (to 0.1rad/s) when their PTO parameters are fully fixed. This implies that adaptive spring-damper control is necessary when the submerged PAs operate at a sea site with a broad wave occurrence spectrum.

IV. CONCLUSIONS

This paper conducted a comparison study in the frequency domain between three submerged PA designs: a generic type as a benchmark and the other two with modified buoy and PTO designs to enhance RCWs. The linearised models for simulation assumed that the displacements of the buoys were small and considered the effects of viscous drag. Constraints were used in PTO optimisation to keep the models within the boundary of linear wave theory.

Results revealed the power absorption mechanisms of the two modified PA designs and compared their engineering characteristics to that of the generic single tether PA from the perspectives of dynamics response, power absorption capability, and PTO design requirements. In comparison to the G1T, the 3T is capable of extracting two to three times power from the combined surge and heave modes across the broad frequency range, given a fixed tether inclination angle set to the optimal value. The economic viability of the 3T largely depends on the feasibility in designing a shared PTO circuit to achieve the desired PTO forces on the three tethers. In contrast, the AMD depends on selecting the appropriate tether length to extract power from the surge mode. It compromises power absorption from the surge and the heave modes for medium frequency waves even if the PTO parameters are tuned to their optimal values. Nevertheless, it still extracts twice the power of the G1T in medium frequency waves. In comparison to the G1T and the 3T, the AMD exhibits larger variations in the optimal PTO parameters across the wave frequencies but demonstrates less requirements for the dynamic PTO force and the tether elongation displacement at medium frequencies. The economic viability of the AMD seems plausible but the costs associated with manufacturing an asymmetric mass distribution buoy and a tower to achieve the desired nominal tether length were ignored in this study. All the three submerged PAs require

adaptive control to operate efficiently in stochastic seas. Future work will compare the PAs in stochastic seas in time-domain subject to directional waves.

ACKNOWLEDGMENT

This research was supported by the Linkage Project LP130100117 funded by the Australian Research Council and the Strategic Research Initiative Fund awarded by the Institute for Mineral and Energy Resources at the University of Adelaide.

REFERENCES

- [1] J. Cruz, *Ocean wave energy: Current status and future perspectives*, Green Energy and Technology, Springer Berlin Heidelberg, Berlin, 2008.
- [2] J. Hayward and P. Osman, "The potential of wave energy," Report, CSIRO, 2011.
- [3] International Energy Agency, "Deploying renewables – Best and future policy practice," Report, International Energy Agency, 2011.
- [4] B. Drew, A.R. Plummer, and M.N. Sahinkaya, "A review of wave energy converter technology," *In Proc. of the Institution of Mechanical Engineers, Part A: Journal of Power and Energy*, vol. 223, no. 8, pp. 887-902, 2009.
- [5] K. Budal and J. Falnes, "A resonant point absorber of ocean-wave power," *Nature*, vol. 256, no. 5517, pp. 478-479, 1975.
- [6] D.V. Evans, "A theory for wave-power absorption by oscillating bodies," *Journal of Fluid Mechanics*, vol. 77, no. 1, pp. 1-25, 1976
- [7] J.N. Newman, *Marine Hydrodynamics*, MIT press, 1977.
- [8] J. Falnes, *Ocean waves and oscillating systems: Linear interactions including wave-energy extraction*, Cambridge University Press, 2002.
- [9] N.Y. Sergiienko, B.S. Cazzolato, B. Ding, P. Hardy, and M. Arjomandi, "Performance comparison of the floating and fully submerged quasi-point absorber wave energy converters," *Renewable Energy*, vol. 108, pp. 425-437, 2017.
- [10] A. Babarit, J. Hals, M. Muliawan, A. Kurniawan, T. Moan, and J. Krokstad, "Numerical estimation of energy delivery from a selection of wave energy converters – final report," Report, Ecole Centrale de Nantes and Norges Teknisk-Naturvitenskapelige Universitet, 2011.
- [11] B. Ding, B.S. Cazzolato, M. Arjomandi, P. Hardy, and B. Mills, "Seastate based maximum power point tracking damping control of a fully submerged oscillating buoy," *Ocean Engineering*, vol. 126, pp. 299-312, 2016.
- [12] F. Meng, A. Rafiee, B. Cazzolato, B. Ding, M. Arjomandi, J. Piper, N.Y. Sergiienko, and Q. Hu, "Numerical simulation of a submerged spherical point absorber with asymmetric mass distribution," *in Proc. of the 12th European Wave and Tidal Energy Conference*, 2017.
- [13] M.A. Srokosz, "The submerged sphere as an absorber of wave power," *Journal of Fluid Mechanics*, vol. 95, no. 4, pp. 717-741, 1979.
- [14] N.Y. Sergiienko, B.S. Cazzolato, B. Ding, and M. Arjomandi, "An optimal arrangement of mooring lines for a three-tether submerged point-absorbing wave energy converter," *Renewable Energy*, vol. 93, pp. 23-37, 2016.
- [15] N.Y. Sergiienko, A. Rafiee, B.S. Cazzolato, B. Ding, and M. Arjomandi, "Feasibility study of the three-tether axisymmetric wave energy converter," *Ocean Engineering*, vol. 150, pp. 221-233, 2018.
- [16] F. Meng, B. Ding, B. Cazzolato, and M. Arjomandi, "Modal analysis of a submerged spherical point absorber with asymmetric mass distribution," *Renewable Energy*, accepted pending minor revision.
- [17] W.E. Cummins, "The impulse response function and ship motions," Report, DTIC Document, 1962.
- [18] J. Morison, J. Johnson, S. Schaaf, "The force exerted by surface waves on piles," *Journal of Petroleum Technology*, vol. 2, no. 5, pp. 149-154, 1950.
- [19] R.D. Blevins, *Applied fluid dynamics handbook*, Krieger Publishing Company, 2003.
- [20] M. Folley, T. Whittaker, and J. van't Hoff, "The design of small seabed-mounted bottom-hinged wave energy converters," *in Proc. of 7th European Wave and Tidal Energy Conference (EWTEC)*, 2007.
- [21] C.M. Linton, "Radiation and diffraction of water waves by a submerged sphere in finite depth," *Ocean Engineering*, vol. 18, no. 12, pp. 61-74, 1991.